Received: 10 December 2021 | Revised: 14 August 2022 | Accepted: 19 August 2022

DOI: 10.1002/htj.22691

ORIGINAL ARTICLE

HEAT TRANSFER WILEY

Direct numerical simulation of "fountain filling box" flow with a confined weak laminar plane fountain

Liqiang Dong[1] | **Wenxian Lin**[1] | **Steven W. Armfield**[2] | **Michael P. Kirkpatrick**[2] | **Nicholas Williamson**[2] | **Mehdi Khatamifar**[1]

[1]College of Science and Engineering, James Cook University, Townsville, Australia

[2]School of Aerospace, Mechanical and Mechatronic Engineering, The University of Sydney, Sydney, New South Wales, Australia

Correspondence
Wenxian Lin, College of Science and Engineering, James Cook University, Townsville, QLD 4811, Australia.
Email: wenxian.lin@jcu.edu.au

Funding information
Australian Research Council; James Cook University

Abstract

A "fountain filling box" flow produced by discharging a weak laminar plane fountain in a confined open channel is studied numerically. Two-dimensional direct numerical simulations were performed for weak plane fountains. The development of the fountain flow experiences five stages; the initial upflow and the subsequent downflow after the fountain penetrates to the maximum height, followed by the outward movement of the intrusion of the fallen fountain fluid on the channel bottom, and then the wall fountain formed by the impingement of the intrusion on the vertical sidewall, which results in the reversed flow, and finally the gradual stratification of the fluid. The behavior of the intrusion can be approximately described with the plane gravity current theory. The period for the intrusion to reach the bounded side wall increases with increasing *Re* or decreasing *Fr*. Three regimes are found for the wall fountain behavior; "no-falling," "slumping down," and "rolling down" behavior. Convection, mixing, conduction, and filling all

contribute to the formation and development of stratification, but their effects vary at different stages. For the initial stages, convection and mixing play a key role, resulting in an increasing bulk entrainment rate, while conduction and filling are dominant after quasi-steady stratification is created, presenting a decreasing bulk entrainment rate.

KEYWORDS
confinement, filling box, intrusion, plane fountain, stratification

1 | INTRODUCTION

A fountain is a buoyant jet with the buoyancy force acting in the opposite direction to its momentum flux at the source, which may result from either the upward discharge of a heavier fluid or the downward discharge of a lighter fluid into an ambient. Under the negative buoyancy, the fountain flow slows down gradually till its front reaches the maximum penetration height. A reversed flow is subsequently formed, falling back as a downflow around the rising upflow in the fountain core. If the downflow remains heavier than its surrounding ambient all the way until it reaches the bottom, it will then move outwards as an intrusion along the bottom floor; but if the downflow has the same density as the ambient at a specific height, it will cease the downward falling and turn its direction to move outward as an intrusion at that height in the ambient.

Fountains are ubiquitous in nature, environmental settings, and industrial applications. Some typical examples include lava flows in magma chambers,[1] volcanic eruption,[2] release of effluent from desalination plants into the ocean,[3] replenishing the cold saline water in solar ponds,[4] elimination of the damage of radiation frost in agriculture using a selective inverted sink (SIS) device,[5] and reverse cycle air-conditioning systems in buildings,[6] to name just a few. The fundamental significance and practical importance of fountains have led to extensive research on fountain flow since the 1950s, and Hunt and Burridge[7] provided a comprehensive review of some key studies on the topic.

A fountain can be distinguished by the form of the fountain source, with a round fountain from a circular source and a plane fountain from a slot source. Fountains can also be classified as very weak, weak, intermediate, forced, and highly forced,[7] or laminar, transition, and turbulent.[8] Furthermore, a fountain behaves substantially differently when its ejection direction varies (vertical or inclined) and when the type and status of the ambient fluid are different (e.g., whether the ambient fluid is quiescent, in motion, homogeneous, stratified, and whether it can mix with the fountain fluid).

The studies on fountains have been predominantly on free fountains in unconfined ambient, as summarized in, for example,[4,7–13] and the fountain penetration height, entrainment, and dilution have been the main characteristic parameters studied. Nevertheless, in many applications, fountains occur in confined environments, and thus the interaction between the fountain flow and the confinement boundaries is inevitable, resulting in substantially different behavior which is currently less understood.

For a typical confined fountain flow, it is seen from Figure 1 that the fountain fluid falls back after the fountain attains its maximum penetration height, subsequently impinges on the base, and then moves outwards as an intrusion. Due to the relatively narrow confinement of the ambient, the intrusion will impinge on the vertical sidewall and move subsequently upwards along the wall to form a plane wall fountain. The wall fountain, which is usually much weaker than the source fountain, will fall back after that due to its larger density to form a reversed flow that moves towards the source, interacting with the intrusion and the ambient fluid on the way. The continuous discharge of the fountain fluid from the source will gradually generate a density stratification of fluid in the confined space. Baines et al.[14,15] denoted such a confined fountain flow as the "fountain filling box model," which is also adopted in the present study.

The characteristics of the "fountain filling box" model share some similarities with those of the "plume filling box" model[15] with overturning, as studied by Kaye and Hunt,[15] particularly the intrusion and the wall fountain.

The "plume filling box model," produced by a plume in a confined region, has received considerable attention because of its fundamental and application significance (e.g., a fire plume in buildings).[16–19] The research has been focused on the behavior of turbulent plumes and the time evolution of density stratification. It has been found that a turbulent plume in a confined space can cause strong flows such as shear flow (i.e., intrusion) resulting from the plume outflow and the overturning structure (i.e., wall fountain) created by the impingement of the intrusion on side boundaries, in the early development stage.[16] Kaye and Hunt[16] developed a theoretical model for an axisymmetric constant-buoyancy-flux turbulent plume in confined cylinders, in which the outflow from the plume was treated as a forced gravity current with constant buoyancy flux, whereas the flow along the sidewall after the impingement of the gravity current is modeled as a wall fountain. Two regimes are identified in terms of the aspect ratio H/W, where W is the cylinder radius and H is its height. For a room with a larger aspect ratio ($H/W > 1.5$), the intrusion is a pure gravity current when impinging on the sidewall, and the rise height of the wall fountain only depends on H. However, for $H/W \leq 1.5$, the intrusion is not fully developed into pure gravity before the impingement, resulting in the wall fountain height depending on both H and W. For $H/W > 4.0$, Barnett[20] found that the upward plume was prevented from impinging on the ceiling due to the downflow in the ambient, and named these "blocked" regimes. Apparently, the secondary flows can in turn affect the behavior of the plumes. In an experimental study on the wall fountain created by a ceiling jet turning

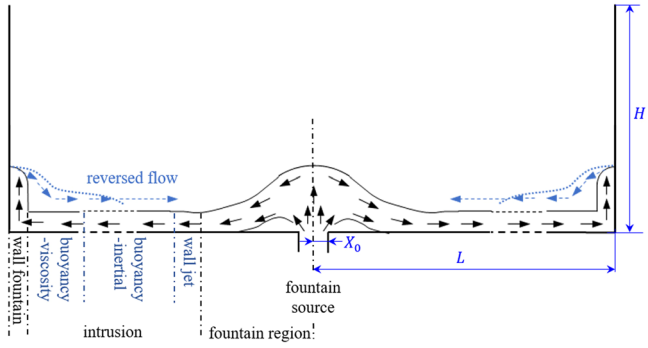

FIGURE 1 Sketches of the "fountain filling box" flow with a confined plane fountain [Color figure can be viewed at wileyonlinelibrary.com]

downward at the corner of a compartment, Jaluria and Kapoor[21] found the penetration depth of the wall fountain only depends on Fr of the outflowing buoyant jet, with a fixed distance between the jet source and the corner. Therefore, the secondary flows and the development of stratification are significantly influenced by the source conditions and the geometry of the confinement.

Due to the similarity to the "plume filling box" model, it is reasonable to expect that the intrusion, wall fountain, and time-dependent density stratification in the "fountain filling box" flow are also influenced by the source condition (via Fr and Re) and the confinement conditions. In their analysis of "fountain filling box" flows with turbulent confined fountains, Baines et al.[14] considered the entrainment but excluded the confinement size. There is a similar knowledge gap for plumes impinging on a density interface. To our best knowledge, only Shrinivas and Hunt[22] took into account the confinement influence on the entrainment of the fountain formed by the impinging plume. In their study, the confinement parameter λ_i is characterized by the ratio of the interfacial turbulence length scale to the depth of the upper layer of the two-layer ambient. When λ_i is small, a weak secondary flow does not influence the entrainment significantly, with the scaling relation $E_i \propto Fr_i^2$, where E_i and Fr_i represent the dimensionless entrainment flux over the interface and the Froude number on the interface respectively, while for large λ_i, $E_i \propto Fr_i^3$.

Recently, there have been some studies focusing on the behavior of fountains under confinement. Debugne and Hunt[23] investigated the impact of the spanwise confinement on turbulent round fountains and identified four flow regimes over $0.5 \le Fr \le 96$ and $2 \le \lambda \le 24$, where $\lambda = W/R_0$ is the dimensionless confinement length, with W the dimensional confinement width and R_0 is the source radius. To account for the effects of confinement, a "confined" Froude number $Fr_c \equiv Fr\lambda^{-5/4}$ was introduced as the governing parameter for confined fountains. Notably, the fountain is only spanwise confined, with no confinement in the lateral direction. Xue et al.[24] characterized the development of round fountains in a bounded container at the initial stage, in terms of Re and Fr over $Re < 500$ and $5 \le Fr \le 35$. Their results show that for a given Fr, the fountain volume entrainment flux ratio attains a local peak at $Re \approx 200$, which is also supported by the measurement of the fountain penetration heights. Their experiments showed that the confinement strengthens the horizontal mixing. However, only two square tanks were tested in their experiments, which makes a systematic study on the impact of the weak confinement impossible. Lippert and Woods[25] examined theoretically and experimentally a particle fountain in a confined environment, and identified four regimes for the flow with different source conditions. Very recently, Dong et al.[26] studied experimentally the behavior of confined laminar and turbulent round "fountain filling box" flow over $1.0 \le Fr \le 20.0$, $102 \le Re \le 1502$, and $27.9 \le \lambda \le 48.75$. We showed that the confinement significantly changes the transient behavior of round fountains in the confined containers, particularly the intrusion, reversed flow, and stratification. We also used three-dimensional direct numerical simulation (DNS) over $0.25 \le Fr \le 3.0$, $5 \le Re \le 800$, and $10 \le \lambda \le 35$ to analyze the intrusion, reversed flow, and stratification of confined weak round fountains[27] and identified three development stages of the bulk entrainment rate. In the present study, our study[27] is extended to the confined weak laminar plane fountains.

The rest of this paper is structured as follows. In Section 2, the details of the DNS runs are provided, including a brief introduction of the physical system. The governing equations, initial and boundary conditions, numerical solution techniques, construction of computational mesh, and the mesh and time-step independence testing are detailed in the accompanying Supporting Information Materials. The snapshots of the contours of temperature obtained from the

numerical results are presented in Section 3 to show the development of the transient flow of typical laminar planar fountains in confined open channels when *Fr*, *Re,* and λ vary. Additionally, the influence of these governing parameters on the confined laminar planar fountains is then analyzed and discussed quantitatively in Section 3, including the movement of the intrusion and wall fountain fronts, the development of stratification, as well as the associated bulk entrainment. The conclusions are finally summarized in Section 4.

2 | NUMERICAL METHODOLOGY

The details of this numerical methodology section are presented in the accompanying Supporting Information Materials. Here only key information is presented. The physical system considered is a two-dimensional (2D) rectangular box of height H and half-width L. The vertical sidewalls of the box are no-slip and adiabatic, and the box top is open. On the center of the bottom floor, a slot of half-width X_0 serves as the source for the 2D plane fountain. The remaining floor area is rigid, no-slip, and adiabatic. Initially, a quiescent homogeneous Newtonian fluid at uniform temperature T_a is filled in the box. At time $t = 0$, a dense jet at temperature T_0 ($T_0 < T_a$) is ejected upward into the box at a velocity W_0 and this discharge is maintained thereafter.

The flow of the 2D laminar plane fountain in a confined homogeneous environment is governed by the 2D incompressible Navier–Stokes equations together with the temperature equation. These governing equations together with the initial and boundary conditions are presented in the Supporting Information Materials.

The main governing parameters are *Re*, *Fr*, and dimensionless length of the rectangular box (λ), which are defined as follows:

$$Re = \frac{W_0 X_0}{\nu}, \tag{1}$$

$$Fr = \frac{W_0}{\sqrt{gX_0(\rho_0 - \rho_a)/\rho_a}} = \frac{W_0}{\sqrt{g\beta X_0(T_a - T_0)}}, \tag{2}$$

$$\lambda = \frac{L}{X_0}, \tag{3}$$

where ρ_0 and ρ_a are the densities of the jet fluid at the source and the ambient fluid, respectively, g is the gravitational acceleration, ρ, β, and ν are the density, volumetric expansion coefficient, and kinematic viscosity of the fluid, respectively. For fountains resulting from the temperature difference between the jet and ambient fluid, *Fr* can also be calculated with the temperature difference using the Oberbeck–Boussinesq approximation for buoyancy, as shown in the second expression in Equation (2), which requires $(\rho_0 - \rho_a)/\rho_a$ to be significantly less than unity.

The discretization and integration of the governing equations are described in the Supporting Information Materials. All direct numerical simulation runs were carried out using ANSYS Fluent 17.0.

A total of 52 DNS runs have been carried out over $0.1 \le Fr \le 3.0$, $5 \le Re \le 800$, and $10 \le \lambda \le 35$, all at $Pr = 7$, with their main data listed in Table 1.

TABLE 1 Key data of the DNS runs

Runs	*Fr*	*Re*	$\lambda \times h$	Mesh
1	0.1	200	20×10	702×334
2	0.15	200	20×10	702×334
3, 4	0.25	100, 200	20×20	1336×531
5, 6, 7, 8	0.5	10, 50, 100, 200	20×20	1336×531
9, 10	0.5	500, 800	20×20	4000×1359
11,12, 13, 14, 15	1	5, 10, 15, 20, 35	20×20	1336×531
16,17, 18, 19, 20	1	50, 75, 100, 150, 200	20×20	1336×531
21, 22, 23, 24, 25	1	300, 400, 500, 600, 800	20×20	4000×1359
26, 27	1.25	100, 200	20×20	1336×531
28, 29, 30, 31	1.5	10, 50, 100, 200	20×20	1336×531
32, 33	1.5	500, 800	20×30	4000×2359
34, 35	1.75	100, 200	20×30	1336×864
36, 37	2	10, 50	20×20	1336×531
38, 39	2	100, 200	20×30	1336×864
40, 41	2	500, 800	20×30	4000×2359
42	2.25	200	20×30	1336×864
43, 44	2.5	100, 200	20×30	1336×864
45	2.75	200	20×30	1336×864
46, 47	3	100, 200	20×30	1336×864
48	1	200	10×30	668×864
49	1	200	15×30	1002×864
50	1	200	25×20	1668×531
51	1	200	30×20	2002×531
52	1	200	35×20	2336×531

The meshes are nonuniform, with fine, uniform grids in the bottom region and a relatively coarse vertically stretched mesh in the top region. Extensive grid and time-step independence tests were conducted to ensure accurate simulation results are produced. Additionally, to ensure the DNS results are accurate, the simulation data for the plane fountain of $0.1 \leq Fr \leq 2.5$ and $Re = 200$ is benchmarked against the existing numerical and experimental data summarized by Hunt and Coffey.[28] These are presented in the Supporting Inforation Materials. The meshes used for each DNS run are also presented in Table 1 where h is the dimensionless height of the rectangular box, which is nondimensionalized by $h = H/X_0$.

3 | RESULTS AND DISCUSSIONS

3.1 | Qualitative observation

3.1.1 | Development of a typical confined laminar plane fountain

In Figure 2, the snapshots of the numerically simulated transient temperature contours are given for the case of $Fr = 0.5$, $Re = 100$, $Pr = 7$, and $\lambda = 20$, providing an overview of the development of a typical confined weak planar fountain. Only the result on the right part of the simulation domain is presented in the figures due to the symmetrical flow behavior of a weak fountain. The results show that there are five development stages, as follows:

1. the initial formation of the free fountain flow and the subsequent fall back after the fountain attains its maximum penetration height ($0 \le \tau \le 1.9$), Figure 2A;
2. the outward movement of the intrusion of the fallen fountain fluid on the domain bottom ($1.9 < \tau \le 11.4$), Figure 2B,C;
3. the wall fountain formed by the intrusion impinging on the sidewall ($16.2 \le \tau \le 19.1$), Figure 2D,E;
4. the reversed flow due to negative buoyancy ($\tau = 21.9$), Figure 2F;
5. the gradual stratification of the fluid in the domain ($\tau \ge 56.2$), Figure 2L.

where τ is the dimensionless time as presented in Supporting Inforation Materials.

After the inception of the fountain flow, the fountain will rise until it attains the maximum height as illustrated in Figure 2A. Since the fountain fluid remains heavier than the ambient fluid, it will then descend to and spread outwards along the bottom, resulting in a layer of denser fluid (intrusion), as illustrated in Figure 2B,C. The intrusion can be treated as a gravity current, with behavior that may be characterized by different regimes in terms of the governing forces, further discussed in Section 3.2.1. Since the evolution of the initial fountain formation and the intrusion was described in Lin and Armfield,[29] the account of these stages is omitted here.

The influence of the bounded sidewall on gravity intrusion becomes significant as the intrusion flow approaches the sidewall. Figure 2D,E show that the circulation above the intrusion head is stretched and spread upwards along the sidewall with the current impinging on the sidewall. Notably, the density of the leaf-like head of the upward flow is significantly smaller than the intrusion current due to the ambient fluid entrained as the intrusion spreads and then impinges on the sidewall. Therefore, the flow could be divided into two regions, that is, the lighter leaf-like region evaluated from the circulation on the top and the heavier flow from the continuous intrusion current at the bottom, as shown in Figure 2E. Since the flow is still heavier than the ambient fluid, the upward flow along the sidewall can be treated as a wall fountain, which keeps moving upwards until a certain height and then slumps back due to the negative buoyancy (Figure 2F). The wall fountain flow behavior will be further discussed in Section 3.2.2. The fallen flow of the wall fountain interacts with the intrusion, resulting in an increase in the thickness of the dense current close to the sidewall region. Additionally, finger-like structures are observed to appear and disappear, as shown in Figure 2G,H. Due to negative buoyancy, a reversed flow is formed, moving from the sidewall to the fountain core as shown in Figure 2G–I. The reversed flow interacts with the sidewall, the intrusion, and the fountain core. As a result, the height of the fountain core experiences a significant increase, until it reaches a

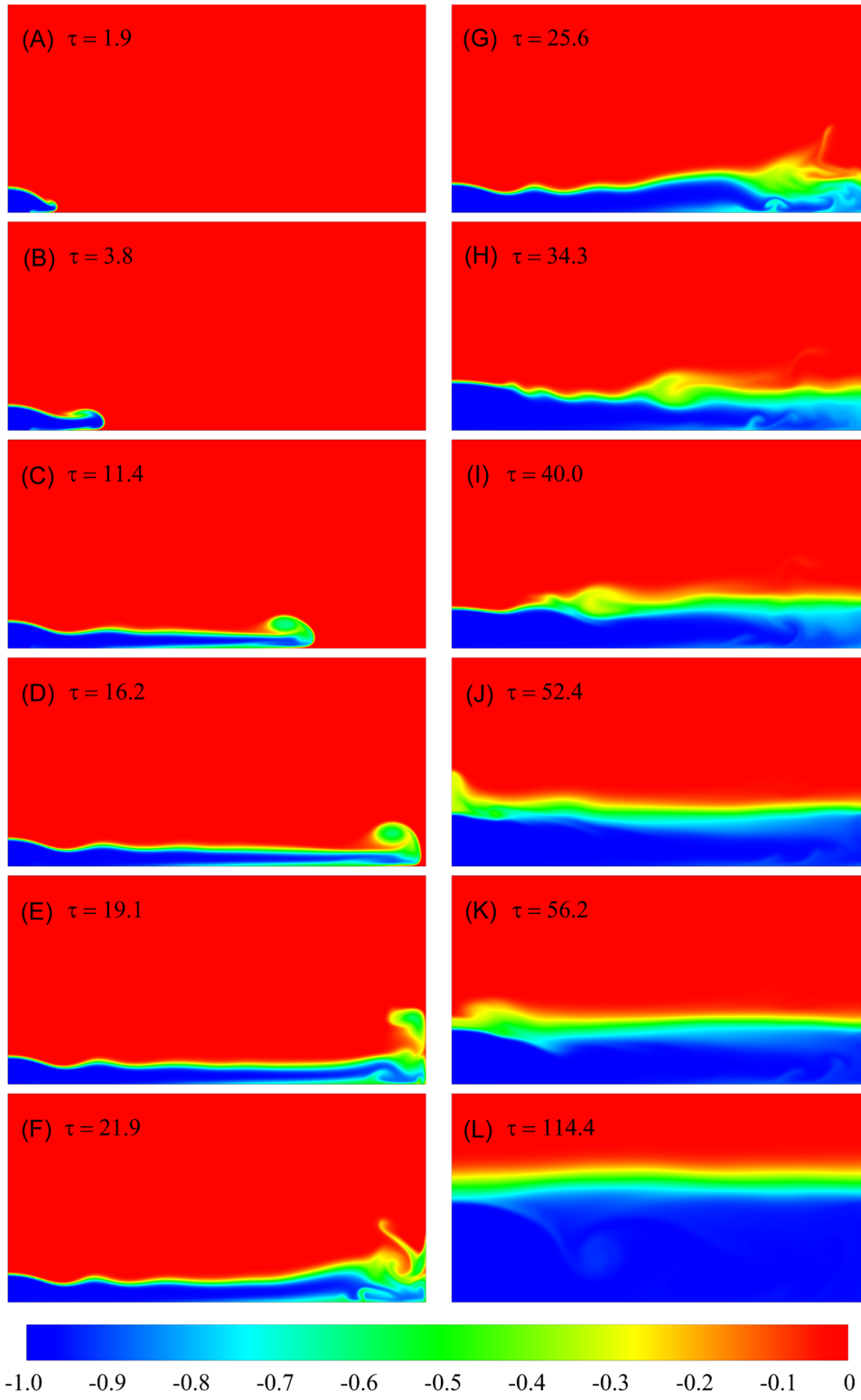

FIGURE 2 (See caption on next page)

certain height, then falls down again due to gravity and creates a stronger intrusion. Figure 2J shows the reversed flow fronts from the sidewall colliding at the center and being projected to a higher position. Due to the negative buoyancy, the flow drops down and separates into the two reversed flow fronts as shown in Figure 2K. This swaying back-and-forth process repeats several times, behaving like a seiche with a decreasing magnitude. After a certain time, a thermal stratification is formed in the domain with the fountain flow submerged, as can be seen in Figure 2L, which grows gradually with time resulting from convection, mixing, thermal conduction, and filling. Particularly, after the fountain is immersed in the stratified fluid, the increase in the stratification height is mainly due to the continual filling of the denser fluid from the source and thermal conduction.

3.1.2 | Influence of *Fr*, *Re,* and λ

The evolution of temperature contours for fountains with $Fr = 0.25$, $Fr = 1.0$ and $Fr = 1.5$, all at $Re = 100$, $Pr = 7$, and $\lambda = 20$, is presented in Figure 3 to display the impact of *Fr*. The first row presents the instant when the intrusion is created. With reference to the nondimensional time units associated with τ, it takes a longer time for the fountain with larger *Fr* to form the intrusion flow. The second and third rows show the time instants when the intrusion flows impinge on the side wall and the wall fountains reach their maximum heights. Thicker intrusion flows, wider jump regions, and higher wall fountain penetration heights are observed for the fountains with larger *Fr*. Additionally, an eddy is observed in the region enclosed by the upflow, the downflow, and the bottom floor for fountains with larger *Fr*. However, it takes longer time for the intrusion with increasing *Fr* to impinge on the sidewall. The fourth and fifth rows show the wall fountains slumping down and the quasi-steady stratification, respectively. It takes longer for the larger *Fr* fountains to form the quasi-steady stratification. The interactions between the intrusion flow, the reversed flow, and the ambient fluid become more significant when *Fr* increases. For brevity, the results of the simulations with other *Fr* values, which show similar behavior, are omitted here, due to the similar development processes.

Figure 4 shows the snapshots of temperature contours for $Fr = 1$, $Pr = 7$, and $\lambda = 20$ with $Re = 20$, $Re = 50$ and $Re = 200$ at different time instants, providing an overview of the impact of *Re* on the long-term behavior of confined weak planar fountains. The time taken for the formation of the intrusion decreases with the increase of *Re* as shown in the first row. The impingement of the intrusion on the sidewall and the maximum penetrations of the wall fountain in the second and third rows show a thinner intrusion flow with an earlier impingement on the sidewall for a larger *Re* fountain. From the third and fourth rows of Figure 4, three regimes are identified for the behavior of the wall fountains. With the increase of *Re*, the shear velocity between the intrusion flow and the ambient increases, resulting in stronger circulation. With the intrusion front approaching and impinging on the side wall, the stronger circulation is stretched to create a more convective upward flow along the side wall. The width of the flow is thinner with the increase of *Re*, resulting in a more significant division between the top region and the bottom region. For the $Re = 50$ case, the division between the top region and the bottom region is not significant, the top region front reaches the maximum height at

FIGURE 2 Temperature contours of the planar fountain with $Fr = 0.5$, $Re = 100$, and $\lambda = 20$ (DNS Run 7) at 12 time instant between $\tau = 1.9$ and $\tau = 114.4$. [Color figure can be viewed at wileyonlinelibrary.com]

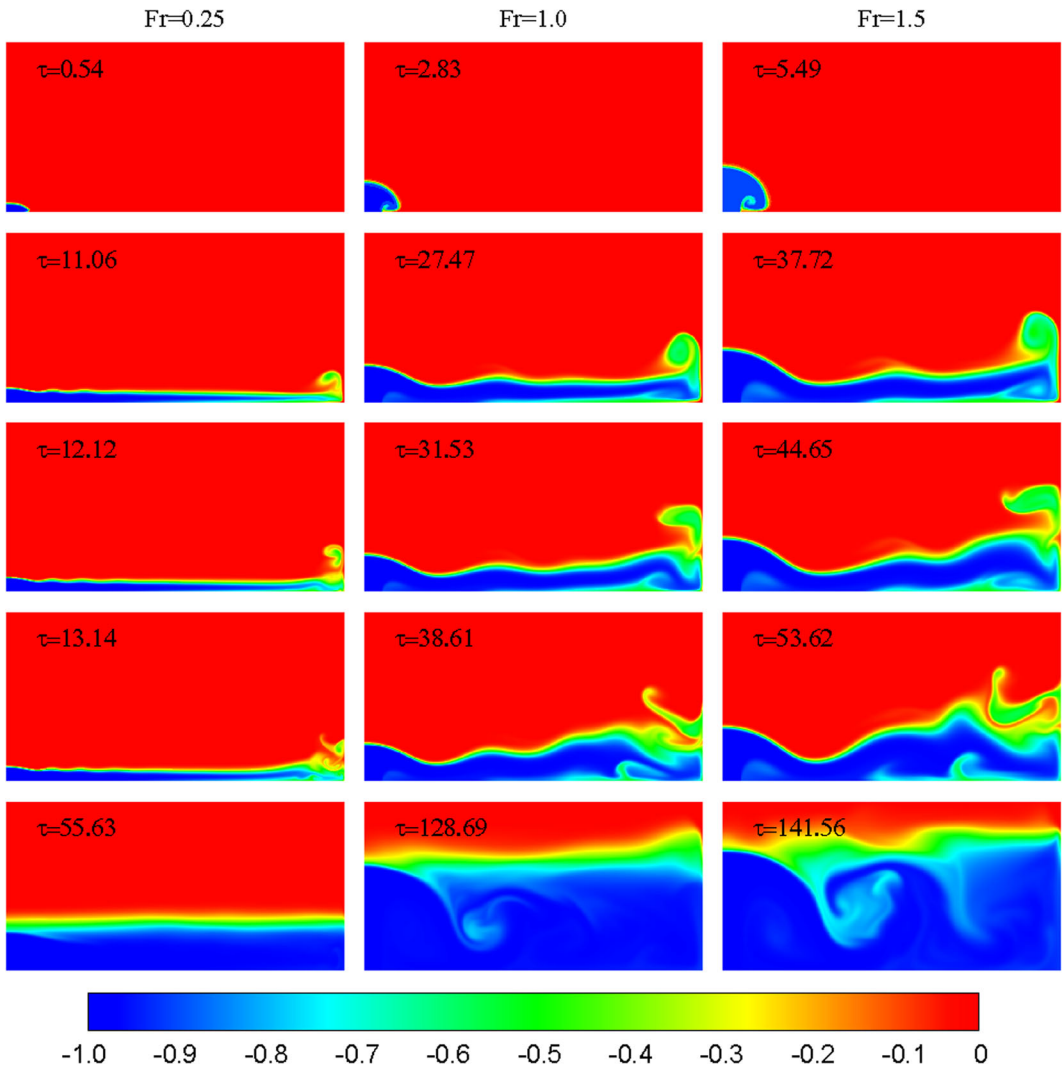

FIGURE 3 Temperature contours of the three fountains of $Fr = 0.25$ (left column, DNS Run 3), $Fr = 1.0$ (middle column, DNS Run 18) and $Fr = 1.5$ (right column, DNS Run 30), all with $Re = 100$ and $\lambda = 20$, at different times. [Color figure can be viewed at wileyonlinelibrary.com]

$\tau = 33.52$ and then slumps down at $\tau = 37.53$. For the $Re = 200$ case, the top region and bottom region are significantly distinguished, with the top region rolling down after reaching the maximum height ($\tau = 31.09$), but its bottom region slumping down. The "slumping down" behavior is similar to that of the "filling box" flow in a large aspect ratio room observed by Kaye and Hunt,[19] while the "rolling down" behavior is determined by the momentum and buoyant flux of the top region. The fountain behavior discussed in this study is focused on the top region. No falling is present for the wall fountain at $Re = 20$, with the reduction in momentum balanced by the stagnation pressure, while a reversed flow is subsequently caused by the negative buoyancy.

For all cases a reversed flow is then created and moves from the sidewall towards the fountain source, interacting with the intrusion flow, the ambient fluid, and the fountain. The interactions become stronger with increasing *Re*. The thickness (height) of the stratification

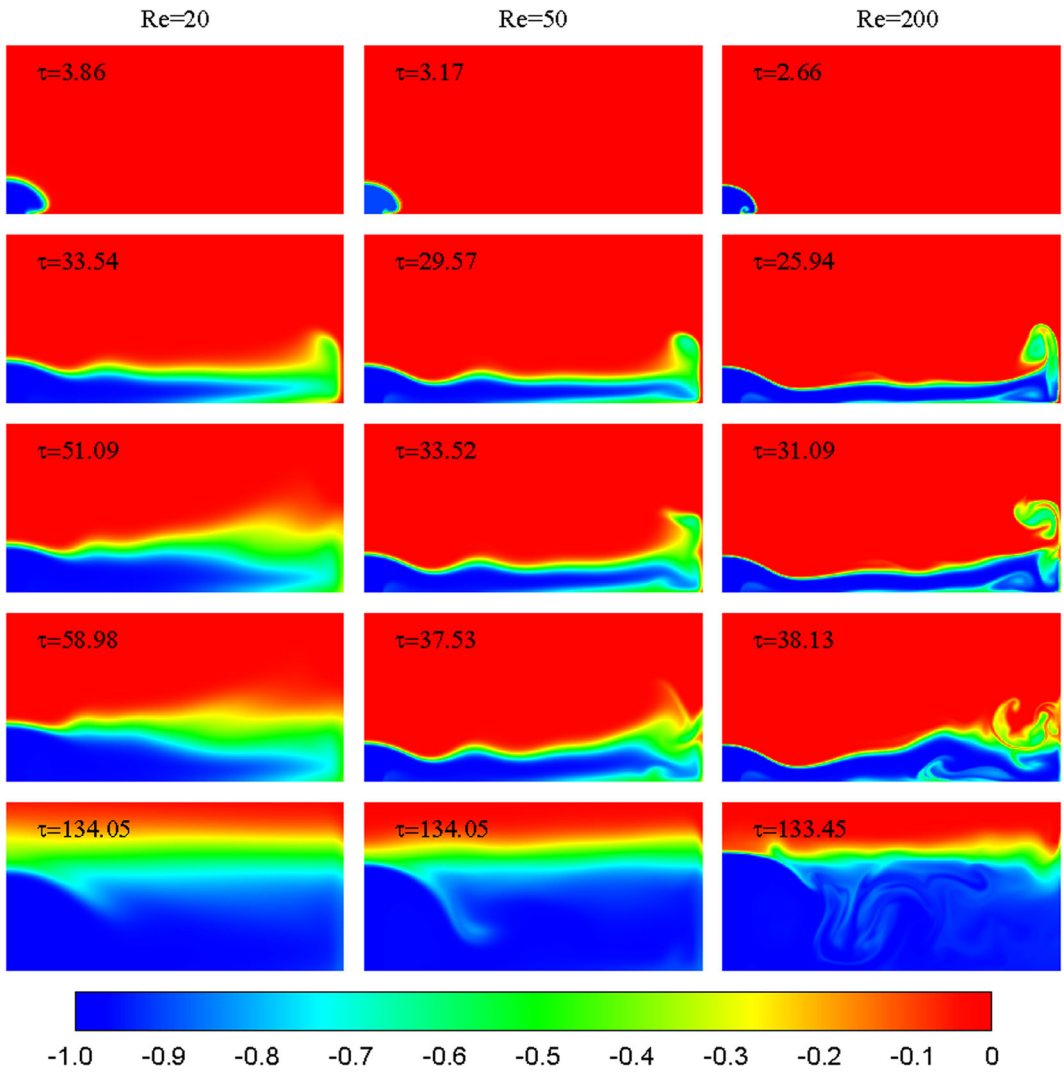

FIGURE 4 Temperature contours of the three fountains of $Re = 20$ (left column, DNS Run 14), $Re = 50$ (middle column, DNS Run 16) and $Re = 200$ (right column, DNS Run 20), all with $Fr = 1.0$ and $\lambda = 20$, at different times. [Color figure can be viewed at wileyonlinelibrary.com]

(the distance between the blue part and the red part) increases with decreasing *Re*, which indicates thermal conduction plays a more significant role.

Figure 5 presents the temperature contours of the $Fr = 1$, $Pr = 7$, and $Re = 200$ fountains with $\lambda = 10$, $\lambda = 20$ and $\lambda = 30$, to display the impact of λ on the wall fountain and filling box flow. A higher maximum height of the wall fountain is attained for the domain with a larger λ. For the domain with $\lambda = 10$, the wall fountain slumps down after it reaches the maximum height at $\tau = 17.34$. While for the domain with $\lambda = 20$ and 30, the wall fountain rolls down after the maximum height position as shown in the middle and right columns. The different falling behavior of the wall fountains between the case of $\lambda = 10$ and the cases of $\lambda = 20$ and 30 is due to the different extents of the associated entrainment in the top region of their wall fountains. For the case of $\lambda = 10$, the associated entrainment is smaller due to a shorter traveling distance, resulting in a more significant

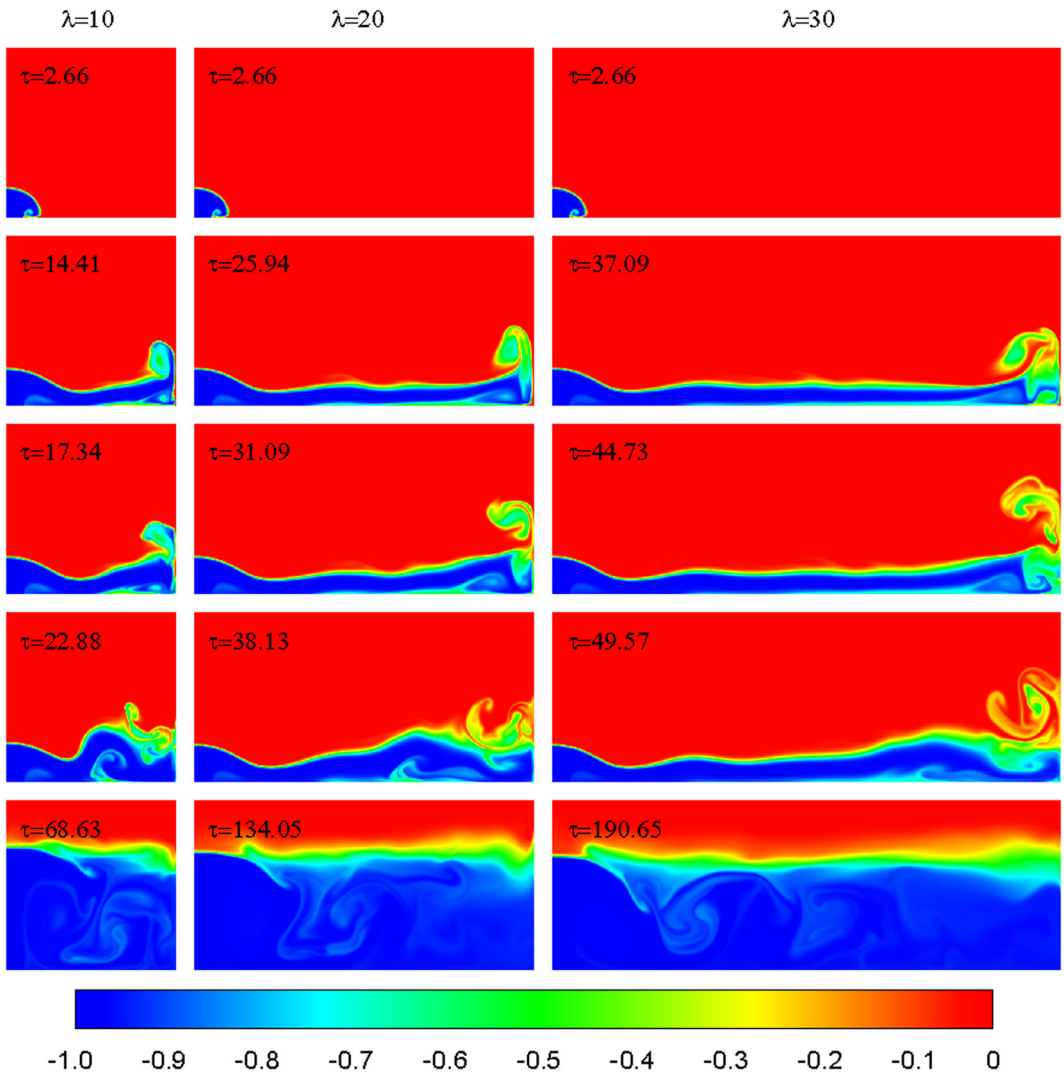

FIGURE 5 Temperature contours of the three fountains of $\lambda = 10$ (left column, DNS Run 48), $\lambda = 20$ (middle column, DNS Run 20) and $\lambda = 30$ (right column, DNS Run 51), all with $Fr = 1.0$ and $Re = 200$, at different times. [Color figure can be viewed at wileyonlinelibrary.com]

negatively buoyant effect. For the domain with a larger λ, it takes longer for the stratified structure to be formed. Similar behavior is observed for $\lambda = 15$, 25, and 35, not shown for brevity.

3.2 | Quantitative observation

3.2.1 | Intrusion

The left column in Figure 6 presents the time series of the movement of the intrusion front for *Fr*, *Re,* and λ over $0.1 \le Fr \le 3.0$, $5 \le Re \le 800$, and $10 \le \lambda \le 35$, respectively. The intrusion front is defined as the *x*-location at which $T(x) = T_a - 1\%(T_a - T_0)$ within the

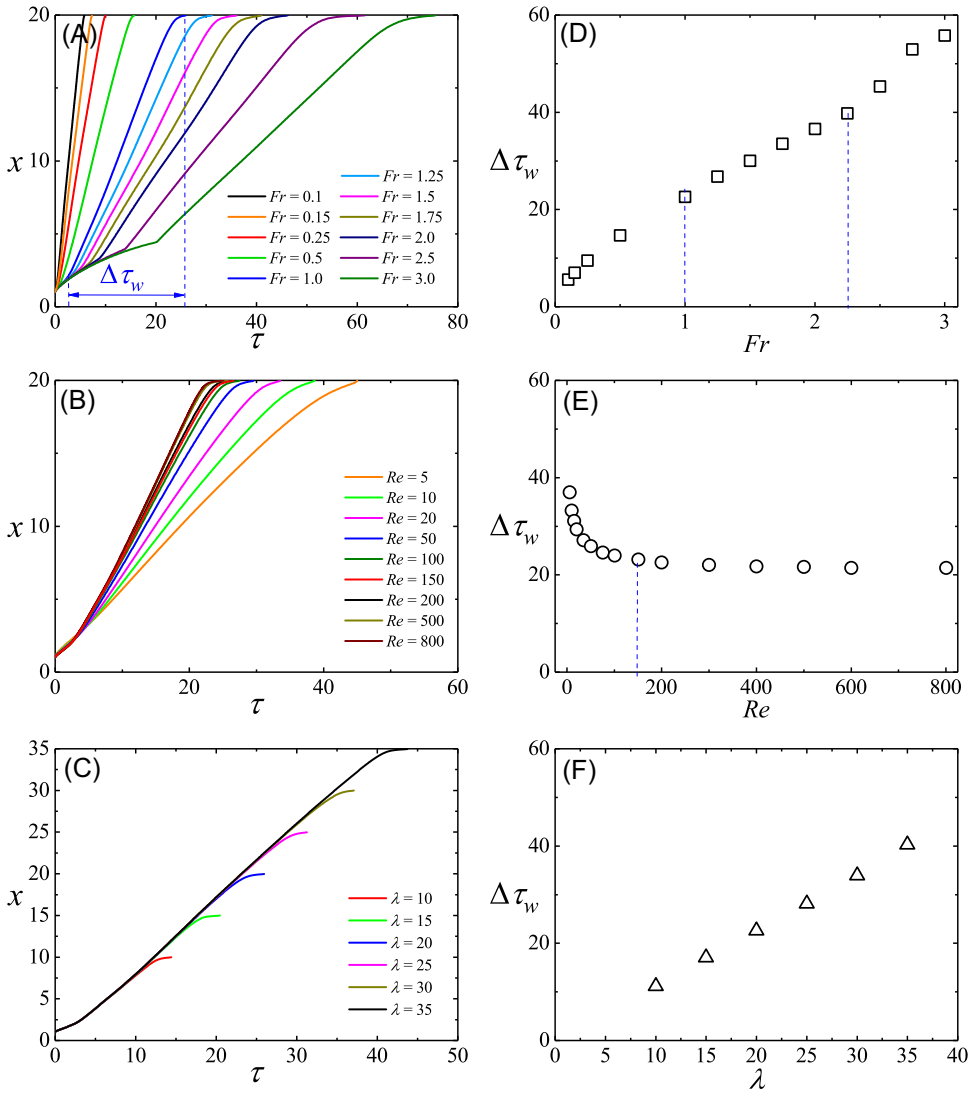

FIGURE 6 (A) The time series of the movement of the intrusion front and (D) $\Delta\tau_w$ versus Fr for different Fr values over $0.1 \le Fr \le 3.0$, all with $Re = 200$ and $\lambda = 20$; (B) the time series of the movement of the intrusion front and (E) $\Delta\tau_w$ versus Re for different Re values over $5 \le Re \le 800$, all with $Fr = 1.0$ and $\lambda = 20$; and (C) the time series of the movement of the intrusion front and (F) $\Delta\tau_w$ versus λ for different λ values over $10 \le \lambda \le 35$, all with $Fr = 1.0$ and $Re = 200$. [Color figure can be viewed at wileyonlinelibrary.com]

right half of the computation domain from $y = 0$ to H. The kink and the endpoints of the time series profile are the instant when the intrusion is created and the instant when the intrusion front impinges on the sidewall, respectively. The period for the intrusion from creation to impinge on the sidewall is denoted as $\Delta\tau_w$, as shown in Figure 6A for the $Fr = 1.0$ result. The results in Figure 6A,B show that it takes a longer time for the intrusion front with larger Fr or smaller Re to impinge on the sidewall. However, the Re dependency reduces with increasing Re, with the $Re = 200$ to $Re = 800$ overlappings, indicating a minimal dependency for $Re \ge 200$. Figure 6C presents the intrusion profiles

for the cases with various confinement sizes λ. It is seen that the effect of the confinement size becomes noticeable only when the intrusion approaches the sidewall.

The impacts of *Fr*, *Re,* and λ on $\Delta\tau_w$ are shown in the right column in Figure 6. From Figure 6D, three ranges can be distinguished with two critical numbers at $Fr = 1.0$ and $Fr = 2.25$. Three corresponding correlations are obtained as follows:

$$\Delta\tau_w = \begin{cases} 22.63Fr^{0.61} - 0.09, 0.1 \le Fr \le 1.0, \\ 13.58Fr + 9.47, 1.0 \le Fr \le 2.25, \\ 22.31Fr - 10.11, 2.25 \le Fr \le 3.0. \end{cases} \tag{4}$$

The regression constants for the three correlations are $R^2 = 1$, 0.998 and 0.974, respectively. Similarly, the influence of *Re* on $\Delta\tau_w$ is presented in Figure 6E. $Re = 150$ is found to distinguish the range into two parts, that is, for $5 \le Re \le 150$, $\Delta\tau_w$ is well approximated by a power law relation, while for $Re \ge 200$, the influence of *Re* on $\Delta\tau_w$ is negligible. The corresponding correlations are determined with the numerical results as follows:

$$\Delta\tau_w = \begin{cases} 46.64Re^{-0.14} - 0.7, 5 \le Re \le 150, \\ 21.82, 200 \le Re \le 800. \end{cases} \tag{5}$$

with a regression constant of $R^2 = 0.991$ for the power relation. Figure 6F shows that $\Delta\tau_w$ has a linear relation with the confinement size of the channel as shown below

$$\Delta\tau_w = 1.14\lambda, 10 \le \lambda \le 35, \tag{6}$$

where the regression constant is $R^2 = 0.999$.

During the development of a pure gravity current, the flow may experience three regimes, that is, the wall jet regime (W-J), the buoyancy-inertial regime (B-I), and the buoyancy-viscosity regime (B-V), which are determined by the dominating forces.[30] For the initial stage, the flow is dominated by momentum as a plane wall jet, so a scaling relation $X(t) \sim M^{1/3}t^{2/3}$ is expected, where *M* is the momentum flux. After that, the driving force of the current becomes buoyancy (gravity) which is balanced by the inertial force, thus the current is in a B-I regime. The balance between the gravity and the inertial force is maintained until the inertial force is small compared to the total viscous drag force resulting from the interfacial shear stress between the current and the ambient fluid and the bottom shear stress, leading to the third regime where the buoyancy force is balanced by the viscous drag force.[30] Two corresponding scaling relations, that is, $X(t) \sim B^{1/3}t$ and $X(t) \sim (BQ^2/\nu)^{1/5}t^{4/5}$, were obtained for the gravity current in the B-I and B-V regimes, respectively,[30] where $Q = X_0W_0$, $B = g(\rho_0 - \rho_a)/\rho_a Q$ are volume and buoyancy fluxes, respectively. The correlations above may be written in dimensionless form as follows:

$$x \sim \tau^{2/3}, \tag{7}$$

for the W-J regime,

$$x \sim Fr^{-2/3}\tau, \tag{8}$$

for the B-I regime, and

$$x \sim Fr^{-2/5} Re^{1/5} \tau^{4/5}, \tag{9}$$

for the B-V regime.

For a free gravity current, Equation (7) indicates that the intrusion front location of the W-J regime is dependent on time, but independent of both *Fr* and *Re*. While for the B-I regime described by Equation (8), the intrusion front presents a linear correlation with time, and only depends on the parameter of *Fr*. In the B-V regime, the correlation follows a power law with time again and is dependent on both *Fr* and *Re*, as shown in Equation (9).

For the fountains with $10 \le \lambda \le 35$, $\Delta\tau_w$ follows a correlation of $\Delta\tau_w \sim \lambda$ as shown in Equation (6). Equation (8) can be transformed into $\tau \sim Fr^{2/3}x$. For the fountain with the same *Fr*, the formula can be further written as $\tau \sim x$, which is consistent with $\Delta\tau_w \sim \lambda$. This indicates that for the cases of $10 \le \lambda \le 35$ with $Fr = 1.0$ and $Re = 200$, the intrusion flows all fall into the B-I regimes.

3.2.2 | Wall fountain

As noted above, the bulk behavior of the wall fountain can be characterized as "No-falling" (i.e., No overturning), "Slumping down," and "Rolling down," as summarized in Figure 7. From this figure, it is found that the overturning behavior of the wall fountain is mainly under the influence of *Re*; for small *Re* values ($5 \le Re \le 20$), no overturning is observed; for $35 \le Re \le 100$, the wall fountain slumps down after reaching the maximum height; and the fountain rolls down for higher *Re* values ($Re \ge 150$). Notably, it is found that the wall fountain for $Fr = 1.0$, $Re = 200$, and $Pr = 7.0$ slumps down when the confinement size reduces to $\lambda = 10$, in contrast to the rolling down behavior for its counterpart of $\lambda \ge 15$. The influence of *Fr* on the overturning behavior is minimal.

To further investigate the influence of these parameters on the wall fountain, the time series of the wall fountain front along the sidewall are presented in Figure 8 (top row). Again, a part of the time series is omitted for clarity. The wall fountain front is defined as the *y*-location

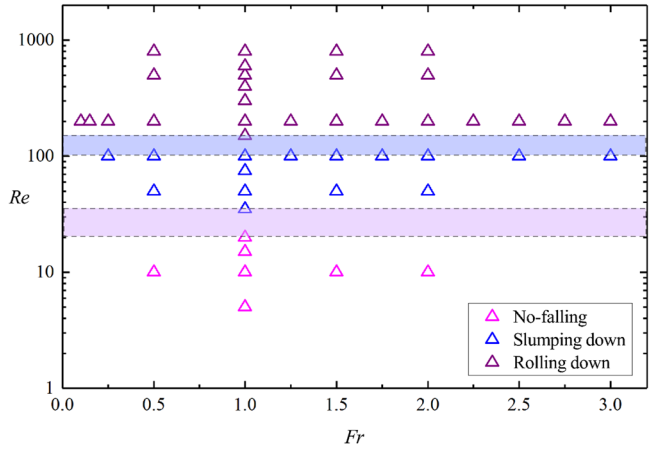

FIGURE 7 Behaviors of the wall fountain for $0.1 \le Fr \le 3.0$, $5 \le Re \le 800$ at $Pr = 7$ and $\lambda = 20$: "No falling," "Slumping down," and "Rolling down." [Color figure can be viewed at wileyonlinelibrary.com]

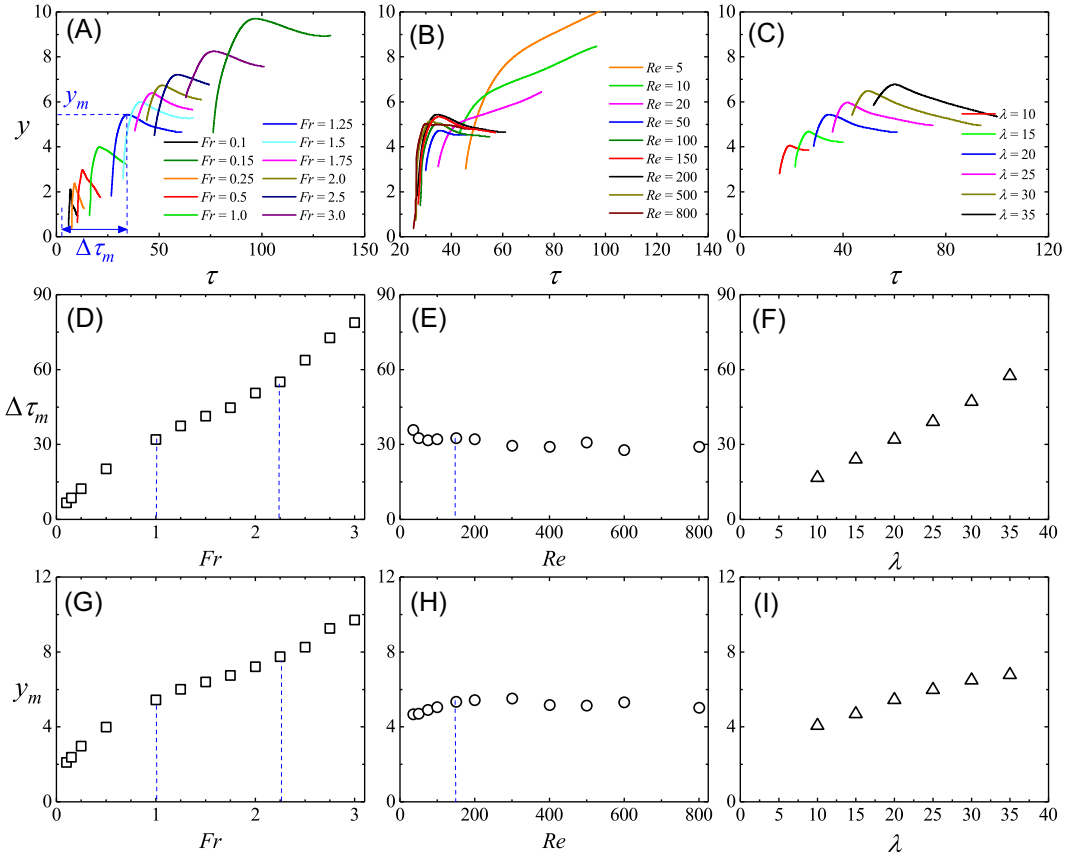

FIGURE 8 The time series of the wall fountain front (top row), $\Delta\tau_w$ (middle row), and y_m (bottom row) for fountains with (A), (D), (G) $Re = 200$, $Pr = 7$, $\lambda = 20$ and $0.1 \le Fr \le 3.0$; (B), (E), (H) $Fr = 1.0$, $Pr = 7$, $\lambda = 20$ and $5 \le Re \le 800$; (C), (F), (I) $Fr = 1.0$, $Re = 200$, $Pr = 7$, and $10 \le \lambda \le 35$. [Color figure can be viewed at wileyonlinelibrary.com]

where $T(y) = T_a - 1\%(T_a - T_0)$ on the sidewall. As shown in Figure 8A, the maximum height of the wall fountain on the sidewall, y_m, is the maximum value of y in the time series and the corresponding, $\Delta\tau_m$, is the period taken for the wall fountain to attain y_m from the creation of the intrusion flow. It is found that y_m increases with Fr and λ but decreases with Re. Similarly, $\Delta\tau_m$ is larger when Fr or λ increases, but becomes smaller when Re increases.

The impact of Fr, Re, and λ on $\Delta\tau_m$ is shown in Figure 8 (middle row). Similar to $\Delta\tau_w$, the impact of Fr on $\Delta\tau_m$ can be divided into three ranges as identified in Figure 8D, with $Fr = 1.0$ and 2.25 as the critical values, and the following correlations are found

$$\Delta\tau_m = \begin{cases} 32.04Fr^{0.69} + 0.07, 0.1 \le Fr \le 1.0, \\ 18.07Fr + 14.16, 1.0 \le Fr \le 2.25, \\ 32.02Fr + 16.47, 2.25 \le Fr \le 3.0. \end{cases} \tag{10}$$

with $R^2 = 1$, 0.995 and 0.993, respectively.

As there is no falling down process for $Re \leq 20$, no $\Delta\tau_m$ exists for these cases. As shown in Figure 8E, it is seen that the impact of Re on $\Delta\tau_m$ can be divided into two different ranges, with $Re = 150$ as the critical value, although the effects of Re on $\Delta\tau_m$ are not significant.

A linear relation is found for the influence of λ on $\Delta\tau_m$, as shown in Figure 8F, which can be approximated by,

$$\Delta\tau_m = 1.6\lambda + 0.03, 10 \leq \lambda \leq 35, \tag{11}$$

with the regression constant of $R^2 = 0.996$.

Figure 8G demonstrates that similar to the impact of Fr on $\Delta\tau_w$ and $\Delta\tau_m$, $Fr = 1.0$ and $Fr = 2.25$ distinguish the impact of Fr on y_m into three different ranges. The corresponding correlations for the three individual ranges are obtained as follows:

$$y_m = \begin{cases} 5.45Fr^{0.42} - 0.05, 0.1 \leq Fr \leq 1.0, \\ 1.78Fr + 3.7, 1.0 \leq Fr \leq 2.25, \\ 2.73Fr + 1.56, 2.25 \leq Fr \leq 3.0. \end{cases} \tag{12}$$

with $R^2 = 0.999$, 0.995 and 0.978, respectively.

From Figure 8H, it is shown that before and after $Re = 150$ Re has different influences on y_m, which is most likely caused by the different overturning behaviors, that is, slumping down for $50 \leq Re \leq 100$ and rolling down for $150 \leq Re \leq 800$.

The influence of λ on y_m can be approximated by,

$$y_m = 0.11\lambda + 3.06, 10 \leq \lambda \leq 35, \tag{13}$$

with $R^2 = 0.984$, which is similar to the impact of λ on $\Delta\tau_m$.

3.2.3 | Stratification

The height of the thermally stratified fluid within the domain is defined as the vertical location where $T(y) = T_a - 1\%(T_a - T_0)$, which is the height of the interface between the stratified fluid produced by the filling of cold fluid through the fountain flow and the ambient fluid. The time series of the maximum, minimum, and average heights of the thermally stratified fluid after the intrusion reaching the sidewall and the establishment of reversed flow are depicted in Figure 9 (left column) for various Fr, Re, and λ. The magnitudes of the differences among these heights are initially significant, due to the key roles played by convection and mixing. After that, over a relatively long time, the differences decrease and the time series of these heights follow essentially the same trend when the filling becomes dominant in the subsequent stratification formation. From this figure, it is seen that the development rate of the quasi-steady stratification can be approximately described by the rate of the averaged stratification height profile.

As shown in Figure 9A, when Fr increases, the magnitudes of the differences among the maximum, average and minimum height profiles increase and a longer time is required for the confined fountain to reach a quasi-steady stratification. Similarly, the differences among these heights increase when Re becomes larger, however, the time to reach a quasi-steady

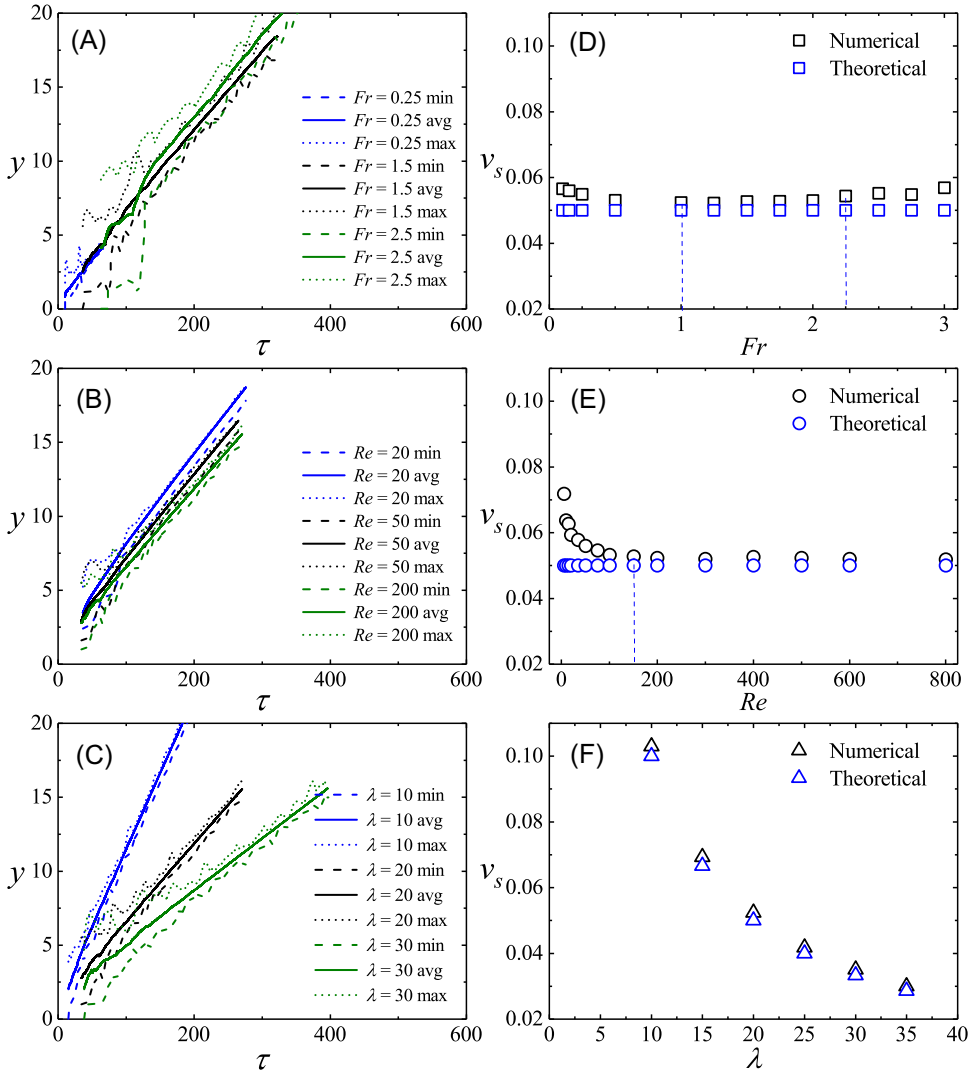

FIGURE 9 The time series of the maximum, minimum and average stratification heights (left column) and v_s (right column) for fountains with (A), (D) $Re = 200$, $Pr = 7$, $\lambda = 20$ and $Fr = 0.25$, 1.5, 2.5; (B), (E) $Fr = 1.0$, $Pr = 7$, $\lambda = 20$ and $Re = 20$, 50, 200; (C), (F) $Fr = 1.0$, $Re = 200$, $Pr = 7$ and $\lambda = 10$, 20, 30. [Color figure can be viewed at wileyonlinelibrary.com]

stratification is decreased. Additionally, the development rate of the stratification decreases with the increase of *Re*.

For a pure filling box without shear flow, convection, mixing, and heat conduction between the filled fluid and the ambient fluid, the velocity of the stratification height, v_s, is the reciprocal of λ ($v_s = 1/\lambda$), based on the conservation of mass. The velocity of the averaged stratification height profile and the corresponding pure filling rate is plotted in Figure 9 (right column) to illustrate the impact of *Fr*, *Re,* and λ on v_s for the fountains filling box. Figure 9D indicates that the impact of *Fr* on v_s, again, can be divided into three ranges by $Fr = 1.0$ and 2.25 as the critical values, although no suitable correlations are obtained.

The influence of Re on v_s, as shown in Figure 9E, can be divided into two different regimes, with $Re = 200$ as the critical value. The results show that,

$$v_s = \begin{cases} 0.051Re^{-0.5} + 0.049, 5 \le Re \le 150, \\ 0.052, 200 \le Re \le 800. \end{cases} \tag{14}$$

As it can be seen, v_s becomes almost independent of Re for Re larger than 150.

The relation between v_s and λ is shown in Figure 9F, and can be approximated by the following correlation:

$$v_s = 0.99\lambda^{-0.98}, 10 \le \lambda \le 35, \tag{15}$$

with the regression constant of $R^2 = 1.0$.

3.2.4 | Bulk entrainment or dilution

Since no assumptions are required for the interactions between the upflow and downflow, or the entrainment process between fountains and surroundings, the bulk entrainment is selected to estimate the mean dilution of the buoyancy scalar over the fountain as a whole instead of resolving the local entrainment rate. The bulk entrainment rate is defined as $\eta = Q_E/Q_0$, where Q_E is the bulk entrainment and Q_0 is the source volume flux. In this study, Q_E is calculated by $Q_E = Q_s - Q_0$, where Q_s represents the volume flux of the stratified fluid. Q_s could be obtained by integrating the area under the thermal stratified surface where the temperature is at $T(y) = T_a - 1\%(T_a - T_0)$ as defined in Section 3.2.3. However, processing the integration for hundreds of thousands of time steps is an excessive workload. Hence, Q_s here is approximated by the product of the x-location and the average thermal stratification height, although a certain error exists for the initial formation of the fountain.

The values of η are calculated for fountains over $0.1 \le Fr \le 3.0$, $5 \le Re \le 800$, and $10 \le \lambda \le 35$, from the intrusion stage to the filling stage. The time series of η, as shown in Figure 10 (top row), can be approximately divided into three stages. First, η increases monotonically until it attains the first peak point which is denoted as η_1. Similarly, the period from the formation of intrusion flow to the instant to attain η_1 is denoted as $\Delta\tau_e$. This stage corresponds to the intrusion development and the evolution of the wall fountain. During the intrusion moving towards the sidewall, the ambient fluid is entrained mainly by the eddy over the intrusion head, resulting in the monotonic increase of η.

After that, η shows a fluctuating decrease with a series of subpeak points. The increases of Fr, Re, and λ strengthen the fluctuations as well as the subpeak points. For most of the cases in this study, η_1 is also the maximum value of η. However, the first peak point decreases with increasing Fr, leading to the role reversal between the first peak and the subpeaks, that is, the "subpeak" point exceeding the first peak point to become the maximum value of η for the case of $Fr = 3.0$, as shown in Figure 10A. Additionally, no obvious fluctuation is observed after the first peak point for the cases of $5 \le Re \le 100$ with $Fr = 1.0$ and $\lambda = 20$, as shown in Figure 10B. However, for the counterpart stage of the cases of $150 \le Re \le 800$, the interactions among the intrusion, the reversed flow, and the ambient fluid induce a fluctuation into the time series until a quasi-steady stratification is established.

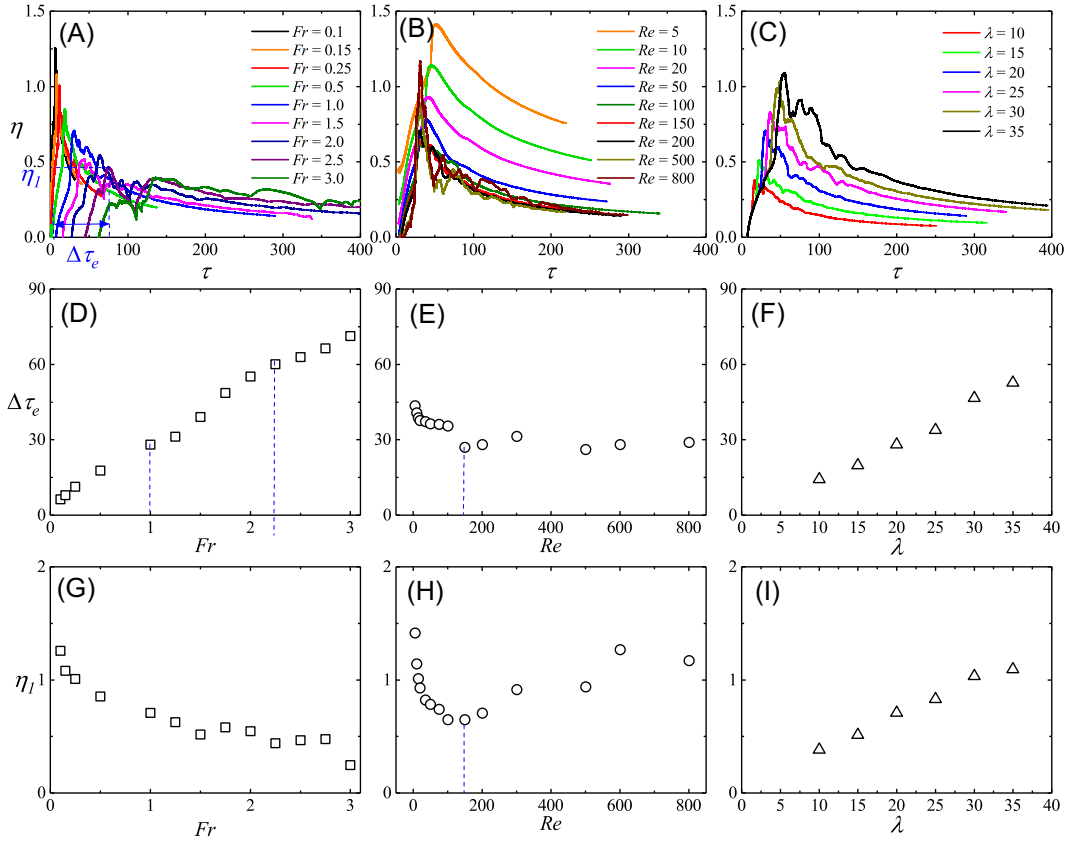

FIGURE 10 The time series of the entrainment rate η (top row), $\Delta\tau_e$ (middle row), and η_m (bottom row) for fountains with (A), (D), (G) $Re = 200$, $Pr = 7$, $\lambda = 20$, and $0.25 \le Fr \le 3.0$; (B), (E), (H) $Fr = 1.0$, $Pr = 7$, $\lambda = 20$, and $5 \le Re \le 800$; (C), (F), (I) $Fr = 1.0$, $Re = 200$, $Pr = 7$, and $10 \le \lambda \le 35$. [Color figure can be viewed at wileyonlinelibrary.com]

With the formation of the quasi-steady stratification, the time series of η finally enters a smooth decline stage. In this stage, entrainment is mainly by thermal conduction, resulting in a decrease of η with the increase of Re and the decreases of Fr and λ. Thermal conduction keeps influencing the dilution process at all stages. The impact of Fr, Re, and λ on η is found to be consistent with the results presented in Section 3.2.3 for the stratification rate.

The influence of Fr, Re, and λ on $\Delta\tau_e$ and η_1 is presented in Figure 10D–F, respectively. Notably, for all the cases except for the one of $Fr = 3.0$ in this study, η_1 could be treated as the maximum value of η, therefore the corresponding $\Delta\tau_e$ can be also determined as the time-scale for the filling flow to reach its maximum entrainment rate. Similarly, $Fr = 1.0$ and $Fr = 2.25$ are determined as the approximate critical values to separate the impact of Fr into three different ranges, with the following correlations obtained,

$$\Delta\tau_e = \begin{cases} 28.11Fr^{0.65} - 0.12, 0.25 \le Fr \le 1.0, \\ 27.61Fr - 1.17, 1.0 \le Fr \le 2.25, \\ 14.89Fr + 26.09, 2.25 \le Fr \le 3.0. \end{cases} \tag{16}$$

with $R^2 = 1.0$, 0.985 and 0.985, respectively. From Figure 10E, $Re = 150$ is determined as the approximately critical value to divide the impact of Re into two ranges, with a power-law correlation obtained for $5 \le Re \le 100$ as follows:

$$\Delta\tau_e = 33.39Re^{-0.83} + 35.09,\ 5 \le Re \le 100, \tag{17}$$

with $R^2 = 0.987$. $\Delta\tau_e$ meets a significant drop for Re increase from $Re = 100$ to $Re = 150$, after which $\Delta\tau_e$ remains approximately constant at an average value $\Delta\tau_e \approx 28.18$, for the cases of $Fr = 1.0$, $\lambda = 20$ with $150 \le Re \le 800$. With the results presented in Figure 10F, the following linear correlation is obtained,

$$\Delta\tau_e = 1.59\lambda - 3.26,\ 10 \le \lambda \le 35, \tag{18}$$

with $R^2 = 0.987$.

η_1 is plotted against Fr, Re, and λ in Figure 10G–I, respectively to depict the impact of these parameters on η_1. The value of η_1 presents a fluctuant decreasing trend with the increase of Fr as shown in Figure 10G. Again, $Re = 150$ is determined as the approximate critical value to divide the impact of Re into two ranges, as shown in Figure 10H. For $5 \le Re \le 100$, η_1 decreases with the increase of Re. However, a fluctuant increasing η_1 is observed for $150 \le Re \le 800$. The influence of λ on η_1 presented in Figure 10I can be quantified by,

$$\eta_1 = 0.029\lambda + 0.087,\ 10 \le \lambda \le 35, \tag{19}$$

with $R^2 = 0.987$.

4 | CONCLUSIONS

The "fountain filling box" flow with a confined weak laminar plane fountain in a confined open channel with a homogeneous ambient fluid is studied using 2D DNS over the ranges $0.1 \le Fr \le 3.0$, $5 \le Re \le 800$, and $10 \le \lambda \le 35$ at $Pr = 7$. The conclusions from the detailed qualitative and quantitative analysis of the behavior of these confined weak laminar plane fountains can be summarized as follows:

- An intrusion current results from the downflow of the fountain impinging on the channel bottom. The behavior of the intrusion flow can be approximately described as a gravity current.[30] The decrease of Fr or the increase of Re can decrease τ_w, that is, the time scales for the intrusion front to impinge on the sidewall.
- Three mechanisms are observed for the behavior of the wall fountain, that is, no-falling (no overturning), slumping down, and rolling down. The maximum penetration height y_m of the wall fountain increases with the increase of Fr and λ, due to the reduction of buoyancy flux.
- For the fountains with $0.1 \le Fr \le 1.0$, $\Delta\tau_w \sim Fr^{0.61}$ and $\Delta\tau_m \sim Fr^{0.69}$ are obtained, where $\Delta\tau_m$ is the period for the wall fountain front to reach its maximum penetration height from the creation of the intrusion flow. For the space with the same dimension, only the buoyancy flux keeps constant, and the time-scale will follow a 2/3 power law with Fr. For $Fr \le 1.0$, the intrusion current spreads fast and remains laminar.

- Convection, filling and conduction all contribute to the formation of thermal stratification. In the initial stage, convection and mixing play a key role. After a quasi-steady stratification is formed, filling and thermal conduction become dominant. The behavior of intrusion and the wall fountain for the fountain at $5 \leq Re \leq 100$, due to its conduction-dominant nature, is significantly different from that at larger *Re* values considered ($150 \leq Re \leq 800$), where convection plays a more significant role. Additionally, $Fr = 1.0$ and $Fr = 2.25$ are found to distinguish the influence of *Fr* into three ranges. With a smaller *Re*, the influence of thermal conduction becomes more significant.
- Compared with the previous DNS results of confined weak round fountains,[27] it is found that it takes a shorter time for the plane fountain than the round one to fill the box of the same dimension, that is, the stratification rate of the plane fountain is larger than that of the round fountain with the same *Fr* and *Re*. Significant instability is observed for the confined weak round fountains during the filling process, however, there is no bobbing or flapping instability observed for the corresponding confined plane fountain.

ACKNOWLEDGMENT

The support from the Australian Research Council is gratefully acknowledged. Liqiang Dong would like to thank James Cook University for the JCUPRS scholarship.Open access publishing facilitated by James Cook University, as part of the Wiley - James Cook University agreement via the Council of Australian University Librarians.

CONFLICT OF INTEREST

The authors declare no conflict of interest.

DATA AVAILABILITY STATEMENT

The data that support the findings of this study are available from the corresponding author upon reasonable request.

ORCID

Wenxian Lin http://orcid.org/0000-0001-5264-2097
Steven W. Armfield http://orcid.org/0000-0002-8032-0017
Nicholas Williamson http://orcid.org/0000-0001-7246-8356
Mehdi Khatamifar http://orcid.org/0000-0001-6273-7655

REFERENCES

1. Campbell IH, Turner JS. The influence of viscosity on fountains in magma chambers. *J Petrol*. 1986;27:1-30.
2. Carazzo G, Kaminski E, Tait S. On the dynamics of volcanic columns: a comparison of field data with a new model of negatively buoyant jets. *J Volcanol Geotherm Res*. 2008;178:94-103.
3. Bleninger T, Jirka GH. Modelling and environmentally sound management of brine discharges from desalination plants. *Desalination* 2008; 221: 585-597.
4. Lin W, Armfield SW. Direct simulation of weak axisymmetric fountains in a homogeneous fluid. *J Fluid Mech*. 2000;403:67-88.
5. Freire D, Kahan S, Cabeza C, Sarasúa G, Marti AC. The formation of coherent structures within turbulent fountains in stratified media. Eur J Mech B Fluids 2015; 50: 89-97.
6. Alajmi A, El-Amer W. Saving energy by using under-floor-air-distribution (UFAD) system in commercial buildings. *Energy Convers Manag*. 2010;51:1637-1642.
7. Hunt GR, Burridge HC. Fountains in industry and nature. *Annu Rev Fluid Mech*. 2015;47:195-220.

8. Williamson N, Srinarayana N, Armfield SW, McBain GD, Lin W. Low-Reynolds-number fountain behaviour. *J Fluid Mech*. 2008;608:297-318.
9. Turner JS. Buoyant plumes and thermals. *Annu Rev Fluid Mech*. 1969;1:295-344.
10. Lin W, Armfield SW. Very weak fountains in a homogeneous fluid. *Numer Heat Transf A*. 2000;38:377-396.
11. Lin W, Armfield SW. The Reynolds and Prandtl number dependence of weak fountains. *Comput Mech*. 2003;31:379-389.
12. Kaye NB, Hunt GR. Weak fountains. *J Fluid Mech*. 2006;558:319-328.
13. Srinarayana N, Williamson N, Armfield SW, Lin W. Line fountain behavior at low-Reynolds number. *Int J Heat Mass Transf*. 2010;53:2065-2073.
14. Baines WD, Turner JS, Campbell IH. Turbulent fountains in an open chamber. *J Fluid Mech*. 1990;212: 557-592.
15. Baines WD, Turner JS. Turbulent buoyant convection from a source in a confined region. *J Fluid Mech*. 1969;37:51-80.
16. Kaye NB, Hunt GR. Overturning in a filling box. *J Fluid Mech*. 2007;576:297-323.
17. Linden PF. The fluid mechanics of natural ventilation. *Annu Rev Fluid Mech*. 1999;31:201-238.
18. Hunt GR, Cooper P, Linden PF. Thermal stratification produced by plumes and jets in enclosed spaces. *Build Environ*. 2001;36:871-882.
19. Kaye NB, Hunt GR. Smoke filling time for a room due to a small fire: the effect of ceiling height to floor width aspect ratio. *Fire Saf J*. 2007;42:329-339.
20. Barnett SJ. The dynamics of buoyant releases in confined spaces. PhD thesis The University of Cambridge. 1992.
21. Jaluria Y, Kapoor K. Wall and corner flows driven by a ceiling jet in an enclosure fire. *Combust Sci Technol*. 1992;86:311-326.
22. Shrinivas AB, Hunt GR. Confined turbulent entrainment across density interfaces. *J Fluid Mech*. 2015;779: 116-143.
23. Debugne ALR, Hunt GR. The influence of spanwise confinement on round fountains. *J Fluid Mech*. 2018;845:263-292.
24. Xue N, Khodaparast S, Stone HA. Fountain mixing in a filling box at low Reynolds numbers. *Phys Rev Fluids*. 2019;4(2):024501.
25. Lippert MC, Woods AW. Particle fountains in a confined environment. *J Fluid Mech*. 2018;855:28-42.
26. Dong L, Lin W, Khatamifar M. Experimental study on the intrusion and stratification produced by confined laminar and turbulent round fountains. *Int J Heat Fluid Flow*. 2021;89:108785.
27. Dong L, Lin W, Khatamifar M. Direct numerical simulation of confined weak round fountains in homogeneous ambient. *Case Stud Therm Eng*. 2021;28:101528.
28. Hunt GR, Coffey CJ. Characterising line fountains. *J Fluid Mech*. 2009;623:317-327.
29. Lin W, Armfield SW. Direct simulation of weak laminar plane fountains in a homogeneous fluid. *Int J Heat Mass Transf*. 2000;43:3013-3026.
30. Chen J-C. Studies on gravitational spreading currents. Ph.D. thesis California Institute of Technology; 1980

SUPPORTING INFORMATION

Additional supporting information can be found online in the Supporting Information section at the end of this article.

How to cite this article: Dong L, Lin W, Armfield SW, Kirkpatrick MP, Williamson N, Khatamifar M. Direct numerical simulation of "fountain filling box" flow with a confined weak laminar plane fountain. *Heat Transfer*. 2022;1-23. doi:10.1002/htj.22691